Optimizing Immuno-PET Imaging of Tumor PD-L1 Expression: Pharmacokinetic, Biodistribution, and Dosimetric Comparisons of ^{89}Zr-Labeled Anti-PD-L1 Antibody Formats

Alizée Bouleau[1], Hervé Nozach[2], Steven Dubois[2], Dimitri Kereselidze[1], Céline Chevaleyre[1], Cheng-I Wang[3], Michael J. Evans[4], Vincent Lebon[1], Bernard Maillère[2], and Charles Truillet[1]

[1]Paris-Saclay University, CEA, CNRS, INSERM, Multimodal Biomedical Imaging Lab, Orsay, France; [2]Paris-Saclay University, CEA, INRAE, Medicines and Healthcare Technologies Department, SIMoS, Gif-sur-Yvette, France; [3]Singapore Immunology Network, A*STAR, Immunos, Singapore, Singapore; and [4]Department of Radiology and Biomedical Imaging, University of California San Francisco, San Francisco, California

PET imaging of programmed cell death ligand 1 (PD-L1) may help to noninvasively predict and monitor responses to anti–programmed cell death 1/anti-PD-L1 immunotherapies. In this study, we compared the imaging characteristics of 3 radioligands derived from the anti-PD-L1 IgG1 complement 4 (C4). In addition to the IgG C4, we produced a fragment antigen-binding (Fab) C4, as well as a double-mutant IgG C4 (H310A/H435Q) with minimal affinity for the murine neonatal Fc receptor. **Methods:** The pharmacokinetics, biodistribution, and dosimetry of the 3 ^{89}Zr-labeled C4 ligands were compared by longitudinal PET/CT imaging in nude mice bearing subcutaneous human non–small cell lung cancer xenografts with positive (H1975 model) or negative (A549 model) endogenous PD-L1 expression. **Results:** The C4 radioligands substantially accumulated in PD-L1–positive tumors but not in PD-L1–negative tumors or in blocked PD-L1–positive tumors, confirming their PD-L1–specific tumor targeting. ^{89}Zr-Fab C4 and ^{89}Zr-IgG C4 (H310A/H435Q) were rapidly eliminated compared with ^{89}Zr-IgG C4. Consequently, maximal tumor-to-muscle ratios were obtained earlier, at 4 h after injection for ^{89}Zr-Fab C4 (ratio, ~6) and 24 h after injection for ^{89}Zr-IgG C4 (H310A/H435Q) (ratio, ~9), versus 48 h after injection for ^{89}Zr-IgG C4 (ratio, ~8). Background activity in nontumor tissues was low, except for high kidney retention of ^{89}Zr-Fab C4 and persistent liver accumulation of ^{89}Zr-IgG C4 (H310A/H435Q) compared with ^{89}Zr-IgG C4. Dosimetry estimates suggested that the C4 radioligands would yield organ-absorbed doses tolerable for repeated clinical PET imaging studies. **Conclusion:** This study highlights the potential of designing radioligands with shorter pharmacokinetics for PD-L1 immuno-PET imaging in a preclinical model and encourages further clinical translation of such radioligands.

Key Words: PET; programmed cell death ligand 1; PD-L1; immunotherapy; pharmacokinetics; non–small cell lung cancer; NSCLC

Immunotherapies with monoclonal antibodies targeting the programmed cell death 1 (PD-1)/programmed cell death ligand 1 (PD-L1) immune checkpoint pathway have significantly improved the treatment of non–small cell lung cancer (NSCLC) (1,2). However, despite remarkable results in some NSCLC patients, only a small subset (~10%–20%) actually responded to anti-PD-1/anti-PD-L1 immunotherapies (3). Therefore, reliable predictive biomarkers of response to PD-1/PD-L1 immune checkpoint inhibitors are urgently needed to guide patient stratification and to maximize therapeutic benefit (4).

PD-L1 expression in NSCLC tumors, determined by immunohistochemistry on biopsy material, was associated with higher response rates to anti-PD-1/anti-PD-L1 immunotherapies (5,6). However, immunohistochemistry evaluation of PD-L1 expression suffers from several limitations that might contribute to the discrepancies observed in treatment response (1). Notably, a single biopsy cannot reflect the spatiotemporal heterogeneity of PD-L1 expression within and across the tumor lesions of a patient (4).

PET with radioligands targeting PD-L1 is a promising approach to complement the conventional immunohistochemistry procedure, as it can provide a holistic, noninvasive, quantitative, and real-time assessment of PD-L1 expression (7). Immuno-PET combines the sensitivity of PET with the high specificity and affinity of radiolabeled antibodies or antibody-derived fragments. Clinical studies involving NSCLC patients have shown encouraging results regarding the predictive value of PD-L1 PET imaging for anti-PD-1/anti-PD-L1 immunotherapies (8,9). In addition to supporting patient selection, PD-L1 PET imaging may also assist in treatment monitoring and response evaluation, facilitating personalized immunotherapy.

A wide range of radioligands targeting PD-L1 has been investigated in preclinical and clinical PET imaging studies (7). Many of these studies used the clinically approved monoclonal antibodies atezolizumab or avelumab, radiolabeled with ^{89}Zr. However, smaller anti-PD-L1 PET radioligands have gained increasing interest. In contrast to full-length antibodies, they can rapidly and deeply diffuse into tumors while being quickly cleared from the blood. As a result, high-contrast images can be obtained within only hours after radioligand administration. Besides size reduction, another strategy for enhancing blood clearance of radiolabeled IgGs relies on altering their binding affinity to the neonatal Fc receptor (FcRn) (10). The FcRn is responsible for the extended plasmatic half-life of IgGs (~21 d), by protecting them from intracellular catabolism through the FcRn-mediated recycling pathway. Introduction of mutations at key amino acid residues in the IgG Fc domain (e.g., I253, H310, and H435) resulted in IgG variants with greatly decreased binding affinity to murine FcRn and significantly faster blood elimination in mice (11–14).

In this comparative study, we investigated 2 different approaches to designing anti-PD-L1 PET radioligands with optimized pharmacokinetic properties. We produced a fragment antigen-binding (Fab) fragment (50 kDa) derived from the antibody complement 4 (C4), a human recombinant IgG1 targeting both human and murine PD-L1. The ^{89}Zr-labeled IgG C4 was previously used for PD-L1 PET imaging in human NSCLC xenograft models and in a patient-derived xenograft model from an NSCLC patient (15). We also engineered a double-mutant IgG C4 (H310A/H435Q) (150 kDa) with minimal affinity for the murine FcRn. The pharmacokinetics, biodistribution, and dosimetry of the ^{89}Zr-labeled IgG C4, IgG C4 (H310A/H435Q), and Fab C4 were evaluated in human NSCLC xenograft models.

MATERIALS AND METHODS

Production of C4 Ligands

The C4 IgG heavy and light chains were cloned into the AbVec2.0-IGHG1 and AbVec1.1-IGLC plasmids, respectively (16). For the Fab C4, the Fc fragment was replaced by a polyhistidine tag. Human HEK293 Freestyle cells (Thermo-Fisher) (2.5×10^6 cells/mL) were transiently cotransfected in 100 mL of Freestyle medium (Thermo-Fisher) by adding 150 μg of each plasmid and 1.8 mL of linear polyethyleneimine (0.5 mg/mL; Polysciences). Cells were incubated for 7 d at 37°C, 120 rpm, and 8% CO$_2$. The culture supernatant was purified using HiTrap Protein A, Lambda-FabSelect, or HisTrap Excel columns (GE Healthcare) for IgG C4, IgG C4 (H310A/H435Q), and Fab C4, respectively. Size-exclusion chromatography was performed using Sephacryl-S-200 HR columns (Sigma) with phosphate-buffered saline.

Biolayer Interferometry

Binding kinetics of the C4 ligands to human PD-L1 (Sinobiological) were determined by biolayer interferometry using an Octet RED96 instrument (ForteBio). AntihIgG Fc Capture Biosensors (Fortebio) were loaded with the IgG C4 (50 nM) for 60 s. Association of human PD-L1 was measured at different concentrations (1.6–100 nM) for 300 s, before dissociation for 1,000 s in kinetic buffer (phosphate-buffered saline with 0.5% bovine serum albumin and 0.05% polysorbate 20). Streptavidin Biosensors (Fortebio) were loaded with biotinylated human PD-L1 (50 nM) for 60 s. Association of Fab C4 was measured at different concentrations (0.78–6.3 nM) for 200 s, before dissociation for 1,000 s in kinetic buffer. Binding curves were fitted to a global 1:1 binding model.

Radiolabeling

The C4 ligands were conjugated with *p*-isothiocyanatobenzyldesferrioxamine (*p*-NCS-Bz-DFO; Macrocyclics) and radiolabeled with ^{89}Zr (PerkinElmer) according to a previously published protocol (17). A 4-fold molar excess of *p*-NCS-Bz-DFO was added to 1 mL of C4 ligand solution (5 mg/mL), and reaction mixture was incubated for 45 min at 37°C. The DFO-C4 ligand conjugates were purified with a PD-10 column (GE Healthcare) using a gentisic acid solution. The DFO-C4 ligand solution was incubated with ^{89}Zr (111 MBq) for 1 h at 37°C. The ^{89}Zr-DFO-C4 ligand conjugates were purified with a PD-10 column using a gentisic acid solution, before being further concentrated and buffer-exchanged in *N*-(2-hydroxyethyl)piperazine-*N'*-(2-ethanesulfonic acid) with a Vivaspin centrifugal concentrator (Sartorius). Radiochemical purity was assessed by instant thin-layer chromatography and size-exclusion high-performance liquid chromatography.

Cell Culture

The human NSCLC cell lines H1975 and A549 were purchased from the American Type Culture Collection. Cells were cultured in RPMI-1640 medium (Gibco) for H1975 cells or Dulbecco modified Eagle medium (Gibco) for A549 cells, supplemented with 10% fetal bovine serum (Gibco) and 1% antibiotic–antimycotic solution (Gibco), at 37°C in a humidified atmosphere with 5% CO$_2$.

Cell Binding Assays

Two million H1975 cells were mixed with ^{89}Zr-IgG C4, ^{89}Zr-IgG C4 (H310A/H435Q), or ^{89}Zr-Fab C4 (2 pmol, 148–296 kBq [4–8 μCi]), with or without a ×100 molar excess of nonradiolabeled C4 ligand. The reaction mixture was incubated for 2 h at 37°C. Cell-associated activity was measured with the Wizard^2 γ-counter (PerkinElmer) and expressed as the percentage total activity added per sample.

Immunoblotting

Total proteins (30 μg) from whole-cell lysates were separated by electrophoresis on Mini-PROTEAN TGX gels (Bio-Rad) and transferred to a polyvinylidene fluoride membrane (Merck Millipore). Blots were incubated with the following primary antibodies: rabbit antihuman PD-L1 (1:1,000, clone E1L3N; Cell Signaling) and rabbit antihuman α-tubulin (1:1,000; Cell Signaling). Blots were then incubated with a horseradish peroxidase–conjugated donkey antirabbit secondary antibody (1:10,000; Jackson ImmunoResearch). Proteins were detected using the Clarity Western ECL Substrate (Bio-Rad). Immunoblots were imaged with the FUSION FX imaging system (Vilber).

Animals

Animal experiments were performed according to the European Directive 2010/63/EU and to its transposition into the French law (decree 2013-118). The research project was conducted at the Comissariat à l'Énergie Atomique–Service Hospitalier Frédéric Joliot imaging platform (authorization D91-471-105) and was approved by a local ethics committee (Comité d'Éthique en Expérimentation Animale du Comissariat à l'Énergie Atomique et aux Énergies Alternatives–Direction des Sciences du Vivant, Ile-de-France). Female nude mice (NMRI-FOXN1 nu/nu; Janvier) were housed in individually ventilated cages in a temperature-controlled (22°C) and humidity-controlled (40%) room, with a 12-h light/12-h dark cycle. Animal experiments were performed under anesthesia with isoflurane in oxygen.

Subcutaneous Injections

Anesthetized mice were subcutaneously inoculated in both lower flanks with H1975 or A549 cells ($4–5 \times 10^6$ cells) suspended in phosphate-buffered saline/Matrigel (BD Biosciences) (1:1). Mice were used for PET imaging studies when tumors reached about 8 mm at the largest diameter.

Small-Animal PET/CT Imaging

Mice (10 ± 1 wk, 27.8 ± 1.4 g) were intravenously injected with the ^{89}Zr-labeled C4 ligands (3.7 ± 0.7 MBq, 7.0 ± 3.0 MBq/nmol, 0.6 ± 0.3 nmol). For blocking studies, mice were coinjected with a ×20 molar excess of nonradiolabeled C4 ligands (1.2 nmol). PET emission scans were performed using an Inveon small-animal PET scanner and an Inveon small-animal PET/CT scanner (Siemens). A 60-min dynamic PET scan was performed immediately after radioligand injection. Twenty-minute static PET scans were subsequently acquired at selected times (4 h, 24 h, 48 h, 72 h, and 7 d) after injection. After each PET scan, a transmission scan or a CT scan was obtained for photon attenuation correction. PET images were reconstructed with Inveon Acquisition Workspace software (version 2.1) using the ordinary Poisson ordered-subsets expectation maximization 3-dimensional maximum a posteriori algorithm. Normalization and corrections for dead time, scatter, decay, and attenuation were applied to all PET data. Volumes of interest were defined with PMOD software (version 3.9). Fixed-size spheric volumes of interest (3.5–8 mm^3) were drawn in representative parts of the heart, liver, and kidneys. Mouse whole-body, spleen, and subcutaneous tumors were delineated semiautomatically.

The mean activity concentration (kBq/cm^3) in each volume of interest was divided by the total injected dose (kBq) to obtain the percentage injected dose per volume of tissue (%ID/cm^3).

Immunohistochemistry

Fixed frozen tumor sections (12 μm) were incubated with a rabbit anti-human PD-L1 primary antibody (1:100, clone E1L3N; Cell Signaling). Slides were then incubated with a horseradish peroxidase–conjugated donkey antirabbit secondary antibody (1:500; Jackson ImmunoResearch). Peroxidase activity was detected with 3–3′-diaminobenzidine (BD Pharmingen). Tumor sections were counterstained with Harris hematoxylin (Sigma-Aldrich). Standard hematoxylin and eosin staining was performed on adjacent tumor sections. Images of stained tumor sections were acquired with the Axio Observer 5 microscope (Zeiss).

Flow Cytometry

Single-cell suspensions were incubated with the following fluorescent-labeled antibodies (10 μg/mL): phycoerythrin-conjugated antihuman PD-L1 antibody (clone 29E.2A3; BioLegend) and phycoerythrin-conjugated mouse IgG2b, κ isotype control (clone MPC-11; BioLegend). For viability assessment, cells were incubated with Zombie Green viability dye (1:500; BioLegend). Flow cytometry was performed on an Attune NxT Acoustic Focusing Cytometer (Invitrogen). Data were analyzed with FlowJo (version 10.7).

Blood Pharmacokinetics

Plasma activity concentrations were calculated from image-derived blood-pool activity concentrations. Considering that antibodies are restricted to the plasma, a blood-to-plasma concentration ratio of 0.55 was used. For each C4 radioligand, plasma time–activity curves of individual mice were pooled and fitted to a 2-compartment model with NONMEM software (version 6.2).

Dosimetry

For each C4 radioligand, residence times (kBq·h·kBq^{-1}) in the main source organs (blood pool, liver, kidneys, spleen, and remainder of body) of individual mice were derived from longitudinal PET images and used in IDAC-Dose software (version 2.1) (18) for human dosimetry estimations. Murine dosimetry was also performed (Supplemental Table 1; supplemental materials are available at http://jnm.snmjournals.org) (19).

Statistics

Statistical analyses were performed with GraphPad Prism (version 9.0.1). A 2-tailed Student t test was used for 2-group data comparison.

RESULTS

Production and Characterization of C4 Radioligands

Biolayer interferometry measurements showed that IgG C4, IgG C4 (H310A/H435Q), and Fab C4 displayed high binding affinities for human PD-L1, with nanomolar affinity constants (Supplemental Fig. 1; Supplemental Table 2). The 3 C4 ligands were successfully conjugated to p-NCS-Bz-DFO and subsequently radiolabeled with ^{89}Zr. Radiochemical purity exceeded 95% in all radiosynthesis experiments (n = 6) (Supplemental Fig. 2; Supplemental Table 3). Endogenous PD-L1 expression on H1975 and A549 cells was confirmed by immunoblotting and flow cytometry (Fig. 1). H1975 cells exhibited high PD-L1 expression compared with A549 cells, with median fluorescence intensity values of 713 ± 56 and 107 ± 7, respectively. In vitro binding assays showed that binding of the ^{89}Zr-labeled C4 ligands to PD-L1–positive H1975 cells was significantly blocked (>70% reduction) by coincubation with an excess of nonradiolabeled ligands, demonstrating the PD-L1 binding specificity of the C4 radioligands (Fig. 1).

Small-Animal PET/CT Imaging with C4 Radioligands in PD-L1–Positive Human NSCLC Xenograft Model

Female nude mice bearing subcutaneous PD-L1–positive H1975 xenografts were injected with the C4 radioligands (3.7 ± 0.7 MBq, 0.6 ± 0.3 nmol), and longitudinal small-animal PET/CT imaging was performed (Supplemental Figs. 3, 4, 5, and 6; Supplemental Tables 4 and 5).

Various blood pharmacokinetic parameters of the C4 radioligands were estimated (Table 1; Supplemental Fig. 7). The ^{89}Zr-Fab C4 fragment exhibited the fastest blood clearance. The Fc-mutant ^{89}Zr-IgG C4 (H310A/H435Q) was also rapidly cleared from circulation as compared with the wild-type ^{89}Zr-IgG C4, with a ×3.4 superior systemic clearance. Remarkably, the estimated biologic elimination half-lives were similar for ^{89}Zr-IgG C4 and ^{89}Zr-IgG C4 (H310A/H435Q). This finding may be explained by the higher retention of ^{89}Zr-IgG C4 (H310A/H435Q) in the peripheral
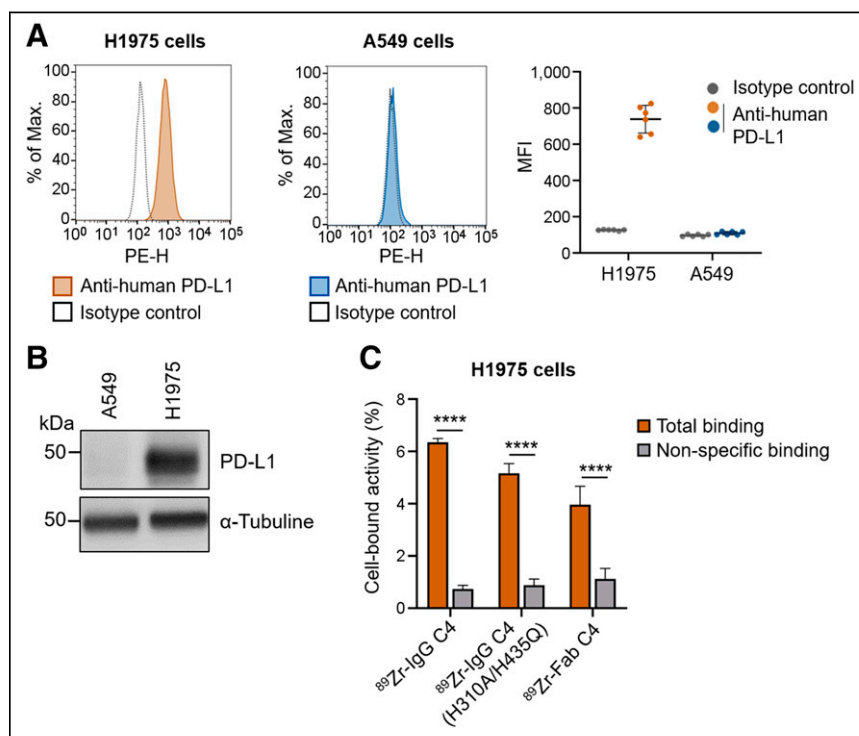

FIGURE 1. Characterization of in vitro PD-L1 expression in human NSCLC cell lines and cell binding assays with C4 radioligands. (A) Representative flow cytometry histograms for cell-surface PD-L1 expression. MFI values are shown on dot plot (6 independent experiments per cell line). (B) Representative immunoblot image showing total PD-L1 expression in whole-cell lysates. (C) Total and nonspecific C4 radioligand binding to PD-L1–positive H1975 cells. Data are mean ± SD, with 6 replicates per condition. Two-tailed paired Student t test was used for data comparison. MFI = median fluorescence intensity; PE-H = phycoerythrin. ****$P < 0.0001$.

TABLE 1
Estimated Blood Pharmacokinetic Parameters

Parameter	^{89}Zr-IgG C4	^{89}Zr-IgG C4 (H310A/H435Q)	^{89}Zr-Fab C4
$t_{1/2\beta}$ (h)	80.25	86.55	1.50
V_c (mL)	2.71	2.41	2.31
CL (mL·h^{-1})	0.047	0.16	2.46
k_{10} (h^{-1})	0.017	0.066	1.06
k_{12} (h^{-1})	0.11	0.08	1.91
k_{21} (h^{-1})	0.12	0.02	1.92
AUC$_{plasma}$ (%ID·h·mL^{-1})	2,137	629	41

$t_{1/2\beta}$ = biologic elimination half-life; V_c = volume of distribution of central compartment; CL = systemic clearance; k_{10} = elimination rate constant from central compartment; k_{12} = distribution rate constant from central to peripheral compartment; k_{21} = distribution rate constant from peripheral to central compartment; AUC$_{plasma}$ = plasmatic exposure.

compartment, as shown by its smaller distribution rate constant from peripheral to central compartment than that of ^{89}Zr-IgG C4.

The 3 C4 radioligands were able to effectively detect PD-L1 expression in H1975 xenografts, but with different tumor uptakes and kinetics (Fig. 2). For ^{89}Zr-IgG C4, optimal PET images were observed at 48 h after injection, with the highest tumor uptake (maximal concentration) being 4.85 ± 0.61 %ID/cm^3, a maximal tumor-to-muscle ratio of 8.34 ± 0.63, and a tumor-to-blood ratio of 0.84 ± 0.35. ^{89}Zr-IgG C4 (H310A/H435Q) tumor accumulation peaked at 24 h after injection, with maximal concentration and maximal tumor-to-muscle ratios similar to those obtained with the ^{89}Zr-IgG C4 (4.60 ± 0.39 %ID/cm^3 and 9.39 ± 0.36, respectively) and a tumor-to-blood ratio of 2.20 ± 1.21. Maximal tumor uptake of ^{89}Zr-Fab C4 was observed even earlier, at 4 h after injection.

However, maximal concentration (1.36 ± 0.11 %ID/cm^3) and maximal tumor-to-muscle ratio (6.28 ± 0.24) were substantially lower, even if the tumor-to-blood ratio was still 1.53 ± 0.85. For the 3 C4 radioligands, H1975 tumor uptake was significantly reduced in mice that received a blocking dose of cold C4 ligand (Fig. 3; Supplemental Table 6), suggesting their PD-L1–specific tumor targeting.

Background activity in most normal tissues was low (Fig. 2). Whereas ^{89}Zr-IgG C4 liver uptake gradually decreased over the imaging time course, ^{89}Zr-IgG C4 (H310A/H435Q) demonstrated high and persistent liver accumulation. The ^{89}Zr-Fab C4 fragment accumulated essentially in the kidneys. This high renal signal retention precluded spleen detection on PET images, and ^{89}Zr-Fab C4 spleen uptake was therefore not quantified.
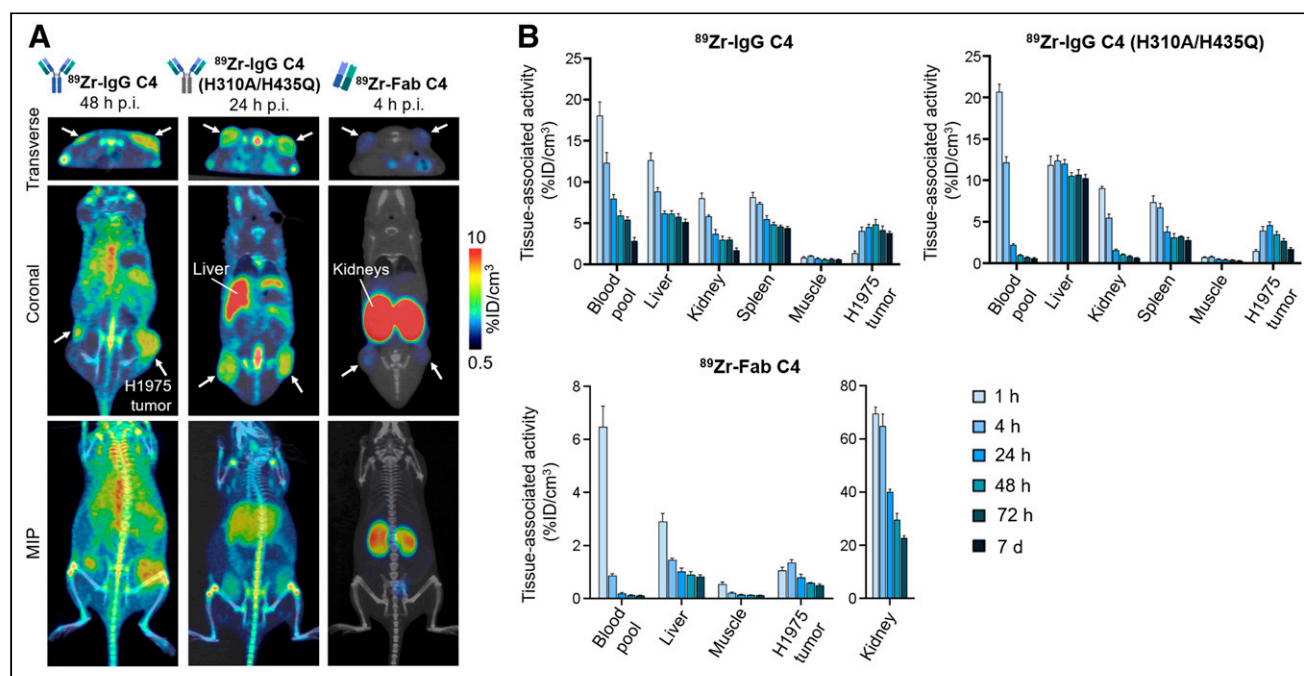

FIGURE 2 Small-animal PET/CT imaging with C4 radioligands in PD-L1–positive human NSCLC xenograft model. (A) Representative small-animal PET/CT image sections and maximum-intensity-projection images of mice bearing PD-L1–positive H1975 xenografts (arrows). (B) Image-derived in vivo biodistribution of C4 radioligands. Data are mean $\pm$ SD, with 6 mice per group. MIP = maximum-intensity projection; p.i. = after injection.
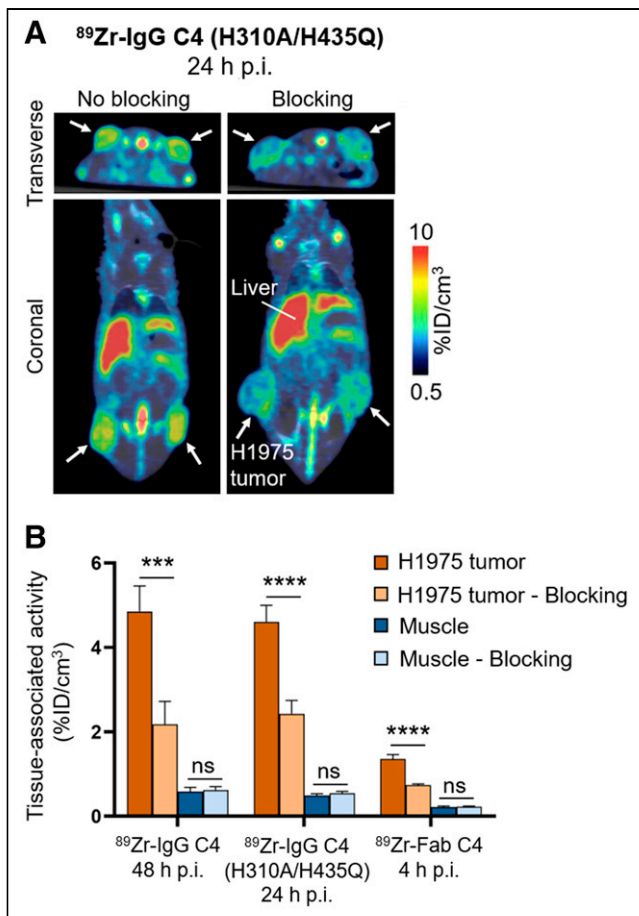
FIGURE 3 PD-L1–specific tumor targeting of C4 radioligands. (A) Representative small-animal PET/CT images of mice bearing PD-L1–positive H1975 xenografts (arrows). (B) Image-derived C4 radioligand uptakes in H1975 tumor and muscle. Data are mean ± SD, with 6 mice per group (no blocking) or 3–4 mice per group (blocking). Two-tailed unpaired Student t test was used for data comparison. ns = not significant. ****P < 0.0001.

For each C4 radioligand, human organ-absorbed dose estimates were extrapolated from murine longitudinal biodistribution data. The highest absorbed doses were in the kidneys and adrenals for ^{89}Zr-Fab C4 and in the liver and heart wall for ^{89}Zr-IgG C4 and ^{89}Zr-IgG C4 (H310A/H435Q) (Supplemental Table 7). The estimated effective doses were 0.34 ± 0.03, 0.35 ± 0.02, and 0.26 ± 0.05 mSv/MBq for ^{89}Zr-IgG C4, ^{89}Zr-IgG C4 (H310A/H435Q), and ^{89}Zr-Fab C4, respectively.

Small-Animal PET/CT Imaging with C4 Radioligands in PD-L1–Positive and PD-L1–Negative Human NSCLC Xenograft Models

The ability of ^{89}Zr-IgG C4 to discriminate between various tumor PD-L1 expression levels was previously demonstrated (15). ^{89}Zr-IgG C4 (H310A/H435Q) and ^{89}Zr-Fab C4 effectively accumulated in PD-L1–positive H1975 xenografts but not in PD-L1–negative A549 xenografts (Fig. 4; Supplemental Fig. 8; Supplemental Table 8). For both radioligands, maximal tumor uptake was about 2-fold higher in H1975 tumors than in A549 tumors. PD-L1 immunohistochemistry showed heterogeneous PD-L1 staining in H1975 tumor sections, whereas very little or no PD-L1 staining was detected in A549 tumor sections (Fig. 4). Flow cytometry corroborated the immunohistochemistry results, with PD-L1–associated median fluorescence

intensity values of 223.9 ± 34.7 versus 72.1 ± 2.5 for the H1975 and A549 tumor cells, respectively (Fig. 4; Supplemental Fig. 9). These ex vivo analyses further validated the in vivo PD-L1–specific tumor targeting of ^{89}Zr-IgG C4 (H310A/H435Q) and ^{89}Zr-Fab C4.

DISCUSSION

The 3 C4 radioligand formats exhibited marked differences in kinetics and in vivo biodistribution patterns, but they were all able to detect PD-L1 expression in human NSCLC xenografts. Although rapid elimination of the ^{89}Zr-Fab C4 fragment gave high-contrast images as soon as 4 h after injection, it also resulted in a poor maximal tumor uptake. Nonetheless, this tumor uptake was similar to that obtained in other preclinical studies performing same-day PET imaging with small anti-PD-L1 radioligands, such as the ^{18}F-labeled adnectin BMS-986192 or small-peptide WL12 (20–23). The faster blood clearance of the Fc-mutant ^{89}Zr-IgG C4 also enabled earlier lesion detection than for the wild-type ^{89}Zr-IgG C4. Unlike ^{89}Zr-Fab C4, the decreased background signal was not accompanied by a reduction in tumor uptake, which remained similar to that of ^{89}Zr-IgG C4. In contrast to the monovalent Fab C4, the Fc-mutant IgG C4 retains 2 binding sites, hence maintaining a strong avidity for tumoral PD-L1. Anti-PD-L1 radioligands with low background activity facilitate the detection of low levels of tumoral PD-L1 expression. This is particularly relevant for clinical PD-L1 PET imaging, as patients with only 1% of PD-L1–positive tumor cells can generate higher response rates to anti-PD-1/PD-L1 immunotherapies than patients with PD-L1–negative tumors (6). Moreover, the H310A/H435Q double mutation has a translational interest because IgG1 binding to human FcRn also involves the conserved H310 and H435 residues (10,14).

Liver accumulation of the ^{89}Zr-labeled IgG C4 was consistent with primary clearance of antibodies through the hepatobiliary system. The increased liver retention obtained with the Fc-mutant ^{89}Zr-IgG C4 was also observed in other preclinical studies that altered the interaction of ^{111}In-labeled IgG1s with the murine FcRn (13,24,25). For instance, Yip et al. generated a mutated variant (H310Q) of a humanized IgG1 with greatly decreased binding affinity to murine FcRn. In immunocompetent mice, liver radioactivity uptake of the ^{111}In-IgG1 (H310Q) at 24 h after injection was about twice higher than that of the parental ^{111}In-IgG1 (13). These results suggested that, in the absence of FcRn protection, the liver emerged as a major site of IgG catabolism in mice.

The ^{89}Zr-Fab C4 fragment was small enough to undergo primarily renal clearance (26). The intense signal retention in the kidneys may be due to reabsorption of the radiolabeled Fab C4 fragment by proximal tubular cells after glomerular filtration. Several strategies have been implemented to reduce such renal accumulation of small radioligands, including coinfusion of basic amino acids that compete with the radioligand for tubular reabsorption (27). PET imaging with the ^{89}Zr-Fab C4 fragment may be particularly adapted for detection of PD-L1 expression in tumor lesions within abdominal organs—lesions that would otherwise be obstructed by the liver clearance signal of the ^{89}Zr-IgGs C4. This is especially relevant for PD-L1 immuno-PET imaging in NSCLC patients, as they are often diagnosed at advanced stages with multiple distant metastases already spread. Approximately 17% of NSCLC patients will develop metastasis in the liver (28).

Because we used immunocompromised mice in this study, the impact of endogenous PD-L1 expression in normal tissues (e.g., lymphoid tissues such as the spleen) on biodistribution and tumor
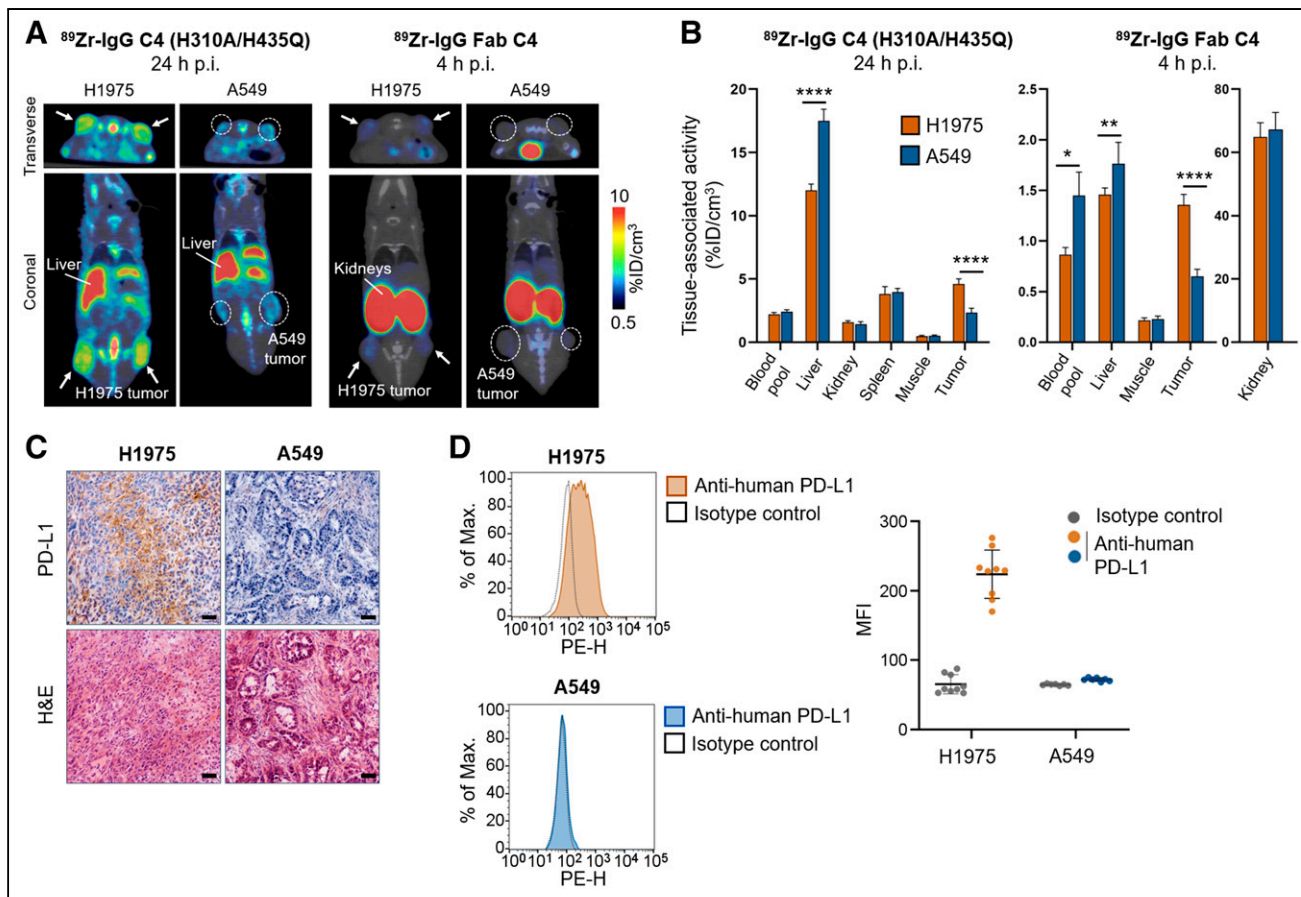
FIGURE 4 Small-animal PET/CT imaging with C4 radioligands in human NSCLC xenograft models with positive or negative PD-L1 expression. (A) Representative small-animal PET/CT images of mice bearing PD-L1–positive H1975 xenografts (arrows) and PD-L1–negative A549 xenografts (dotted circles). (B) Image-derived in vivo biodistribution of C4 radioligands. Data are mean ± SD, with 5–6 mice per group. Two-tailed unpaired Student t test was used for data comparison. (C) Representative images of tumor sections after PD-L1 immunohistochemistry and hematoxylin and eosin staining after imaging. Scale bars = 50 μm. (D) Representative flow cytometry histograms for cell-surface PD-L1 expression on tumor-derived single-cell suspensions. MFI values are shown on dot plot (9 H1975 tumors, 7 A549 tumors). H&E = hematoxylin and eosin; MFI = median fluorescence intensity; PE-H = phycoerythrin; p.i. = after injection. *$P < 0.05$. **$P < 0.01$. ****$P < 0.0001$.

targeting of the C4 radioligands could not be properly evaluated. Thanks to its cross-reactivity with murine PD-L1, the [89]Zr-labeled IgG C4 has already been evaluated in a syngeneic mouse model of melanoma (B16-F10) (15). Surprisingly, no notable differences in radioligand uptake within normal tissues were observed between the B16-F10 tumor–bearing immunocompetent mice and the H1975 tumor–bearing immunocompromised mice.

The estimated human effective doses for the 3 C4 radioligands were in the same range as the values obtained in clinical immuno-PET studies using other [89]Zr-labeled antibodies. Administration of 37 MBq in patients, as already performed in a clinical study with [89]Zr-atezolizumab (8), would result in effective doses of about 13 mSv for the [89]Zr-IgG C4 and of about 10 mSv for the [89]Zr-Fab C4. By comparison, the effective dose of a ^{18}F-FDG PET scan is about 6–7 mSv (29). The favorable dosimetry of the C4 radioligands may enable repeated PD-L1 immuno-PET imaging, as would be required for treatment response monitoring. Moreover, thanks to its faster pharmacokinetics, the Fab C4 may be radiolabeled with a shorter-lived PET isotope such as ^{18}F, which would minimize the patient radiation burden.

CONCLUSION

The [89]Zr-labeled Fab C4 fragment and Fc-mutant IgG C4 enabled specific and efficient detection of PD-L1 expression in a human NSCLC xenograft model at earlier time points than for the parental [89]Zr-labeled IgG C4. This study demonstrated the feasibility of designing anti-PD-L1 radioligands with enhanced imaging characteristics for PD-L1 immuno-PET imaging in preclinical models and supports the clinical translation of such engineering approaches.

DISCLOSURE

ACKNOWLEDGMENTS

KEY POINTS

QUESTION: How can immuno-PET imaging of PD-L1 expression be optimized in NSCLC patients?

PERTINENT FINDINGS: A Fab fragment and a double-mutant IgG (H310A/H435Q) with minimal affinity for murine FcRn were derived from the anti–PD-L1 IgG1 C4. The [89]Zr-labeled Fab C4 and IgG C4 (H310A/H435Q) enabled effective detection of PD-L1 expression by PET imaging in a human NSCLC xenograft model, at earlier time points than for the parental [89]Zr-labeled IgG C4.

IMPLICATIONS FOR PATIENT CARE: These results highlight the possibility of designing anti–PD-L1 PET radioligands with optimized pharmacokinetic properties, to better predict and monitor responses to anti–PD-1/anti–PD-L1 immunotherapies with PD-L1 immuno-PET.

REFERENCES

1. Constantinidou A, Alifieris C, Trafalis DT. Targeting programmed cell death-1 (PD-1) and ligand (PD-L1): a new era in cancer active immunotherapy. *Pharmacol Ther.* 2019;194:84–106.

2. Yang C-Y, Yang JC-H, Yang P-C. Precision management of advanced non–small cell lung cancer. *Annu Rev Med.* 2020;71:117–136.

3. Sun C, Mezzadra R, Schumacher TN. Regulation and function of the PD-L1 checkpoint. *Immunity.* 2018;48:434–452.

4. Nishino M, Ramaiya NH, Hatabu H, Hodi FS. Monitoring immune-checkpoint blockade: response evaluation and biomarker development. *Nat Rev Clin Oncol.* 2017;14:655–668.

5. Passiglia F, Bronte G, Bazan V, et al. PD-L1 expression as predictive biomarker in patients with NSCLC: a pooled analysis. *Oncotarget.* 2016;7:19738–19747.

6. Herbst RS, Baas P, Kim D-W, et al. Pembrolizumab versus docetaxel for previously treated, PD-L1-positive, advanced non-small-cell lung cancer (KEYNOTE-010): a randomised controlled trial. *Lancet.* 2016;387:1540–1550.

7. Bouleau A, Lebon V, Truillet C. PET imaging of immune checkpoint proteins in oncology. *Pharmacol Ther.* 2021;222:107786.

8. Bensch F, van der Veen EL, Lub-de Hooge MN, et al. [89]Zr-atezolizumab imaging as a non-invasive approach to assess clinical response to PD-L1 blockade in cancer. *Nat Med.* 2018;24:1852–1858.

9. Niemeijer AN, Leung D, Huisman MC, et al. Whole body PD-1 and PD-L1 positron emission tomography in patients with non-small-cell lung cancer. *Nat Commun.* 2018;9:4664.

10. Pyzik M, Sand KMK, Hubbard JJ, Andersen JT, Sandlie I, Blumberg RS. The neonatal Fc receptor (FcRn): a misnomer? *Front Immunol.* 2019;10:1540.

11. Kim J-K, Firan M, Radu CG, Kim C-H, Ghetie V, Ward ES. Mapping the site on human IgG for binding of the MHC class I-related receptor, FcRn. *Eur J Immunol.* 1999;29:2819–2825.

12. Kenanova V, Olafsen T, Crow DM, et al. Tailoring the pharmacokinetics and positron emission tomography imaging properties of anti–carcinoembryonic antigen single-chain Fv-Fc antibody fragments. *Cancer Res.* 2005;65:622–631.

13. Yip V, Palma E, Tesar DB, et al. Quantitative cumulative biodistribution of antibodies in mice: effect of modulating binding affinity to the neonatal Fc receptor. *MAbs.* 2014;6:689–696.

14. Burvenich IJG, Parakh S, Lee F-T, et al. Molecular imaging of T cell co-regulator factor B7-H3 with [89]Zr-DS-5573a. *Theranostics.* 2018;8:4199–4209.

15. Truillet C, Oh HLJ, Yeo SP, et al. Imaging PD-L1 expression with immunoPET. *Bioconjug Chem.* 2018;29:96–103.

16. Smith K, Garman L, Wrammert J, et al. Rapid generation of fully human monoclonal antibodies specific to a vaccinating antigen. *Nat Protoc.* 2009;4:372–384.

17. Vosjan MJWD, Perk LR, Visser GWM, et al. Conjugation and radiolabeling of monoclonal antibodies with zirconium-89 for PET imaging using the bifunctional chelate p-isothiocyanatobenzyl-desferrioxamine. *Nat Protoc.* 2010;5:739–743.

18. Andersson M, Johansson L, Eckerman K, Mattsson S. IDAC-Dose 2.1, an internal dosimetry program for diagnostic nuclear medicine based on the ICRP adult reference voxel phantoms. *EJNMMI Res.* 2017;7:88.

19. Locatelli M, Miloudi H, Autret G, et al. RODES software for dose assessment of rats and mice contaminated with radionuclides. *J Radiol Prot.* 2017;37:214–229.

20. Wei J, Wang Y, Lee CY, et al. An analysis of isoclonal antibody formats suggests a role for measuring PD-L1 with low molecular weight PET radiotracers. *Mol Imaging Biol.* 2020;22:1553–1561.

21. Donnelly DJ, Smith RA, Morin P, et al. Synthesis and biologic evaluation of a novel ^{18}F-labeled adnectin as a PET radioligand for imaging PD-L1 expression. *J Nucl Med.* 2018;59:529–535.

22. Stutvoet TS, van der Veen EL, Kol A, et al. Molecular imaging of PD-L1 expression and dynamics with the adnectin-based PET tracer ^{18}F-BMS-986192. *J Nucl Med.* 2020;61:1839–1844.

23. Lesniak WG, Mease RC, Chatterjee S, et al. Development of [^{18}F]FPy-WL12 as a PD-L1-Specific PET imaging peptide. *Mol Imaging.* 2019;18:1536012119852189.

24. Jaggi JS, Carrasquillo JA, Seshan SV, et al. Improved tumor imaging and therapy via i.v. IgG–mediated time-sequential modulation of neonatal Fc receptor. *J Clin Invest.* 2007;117:2422–2430.

25. Kenanova V, Olafsen T, Williams LE, et al. Radioiodinated versus radiometal-labeled anti–carcinoembryonic antigen single-chain Fv-Fc antibody fragments: optimal pharmacokinetics for therapy. *Cancer Res.* 2007;67:718–726.

26. Xenaki KT, Oliveira S. van Bergen en Henegouwen PMP. Antibody or antibody fragments: implications for molecular imaging and targeted therapy of solid tumors. *Front Immunol.* 2017;8:1287.

27. Vegt E, de Jong M, Wetzels JFM, et al. Renal toxicity of radiolabeled peptides and antibody fragments: mechanisms, impact on radionuclide therapy, and strategies for prevention. *J Nucl Med.* 2010;51:1049–1058.

28. Zhu T, Bao X, Chen M, et al. Mechanisms and future of non-small cell lung cancer metastasis. *Front Oncol.* 2020;10:585284.

29. Martí-Climent JM, Prieto E, Morán V, et al. Effective dose estimation for oncological and neurological PET/CT procedures. *EJNMMI Res.* 2017;7:37.